RSC Advances

PAPER

View Article Online
View Journal | View Issue

Cite this: *RSC Adv.*, 2021, **11**, 12507

Dextran mediated $MnFe_2O_4$/ZnS magnetic fluorescence nanocomposites for controlled self-heating properties

D. K. Mondal, Sarodi Jonak, N. Paul and J. P. Borah *

Dextran mediated $MnFe_2O_4$/ZnS opto-magnetic nanocomposites with different concentrations of ZnS were competently synthesized adopting the co-precipitation method. The structural, morphological, magnetic, and optical properties of the nanocomposites were exhaustively characterized by XRD, HRTEM, FTIR, VSM techniques, and PL spectroscopy. XRD spectra demonstrate the existence of the cubic spinel phase of $MnFe_2O_4$ and the cubic zinc blend phase of ZnS in the nanocomposites. HRTEM images show the average crystallite size ranges of 15–21 nm for $MnFe_2O_4$ and 14–45 nm for ZnS. Investigation of the FTIR spectra reveals the incorporation of ZnS nanoparticles on the surface of $MnFe_2O_4$ nanoparticles by dint of biocompatible surfactant dextran. The nanocomposites exhibit both magnetic and photoluminescence properties. Photoluminescence analysis confirmed the redshift of the emission peaks owing to the trap states in the ZnS nanocrystals. The room temperature VSM analysis shows that the saturation magnetization and coercivity of $MnFe_2O_4$ nanoparticles initially increase then decrease with the increasing concentration of ZnS in the nanocomposite. The induction heating analysis shows that the presence of dextran enhances the self heating properties of the $MnFe_2O_4$/ZnS nanocomposites which can also be controlled by tailoring the concentration of the ZnS nanoparticles. These suggest that $MnFe_2O_4$/Dex/ZnS is a decent candidate for hyperthermia applications.

Received 17th November 2020
Accepted 23rd March 2021

DOI: 10.1039/d0ra09745d

rsc.li/rsc-advances

1. Introduction

The research on magnetic/fluorescent nanocomposites has attained significant potential in numerous technological applications such as catalysis,[1–5] devices,[6–12] and so on.[13–19] Recently, due to their exciting magnetic and optical properties the development of opto-magnetic nanocomposites has provided new opportunities for biomedical application such as effective targeted and real-time monitoring drug delivery systems,[20] labelling tissues *in vivo* for MRI imaging,[21] fluorescent markers used to track the migration and anchoring of drugs in cells[22–24] and magnetic hyperthermia.[25–28] Superparamagnetic spinel ferrite (MFe_2O_4 where M = Mn, Ni, Co, Zn, *etc.*) nanoparticles are exceptional for hyperthermia applications due to their high biocompatibility, chemical stability, and the possibility to fine-tune their superparamagnetic properties by chemical manipulation. In the series of mixed spinel ferrites, $MnFe_2O_4$ is a strong contestant, which has been extensively used for efficient magnetic hyperthermia,[29–31] targeted drug delivery and in MRI contrast agents.[32] The $MnFe_2O_4$ nanoparticles have a mixed spinel structure having a degree of inversion $\delta = 0.2$ and their structural formula is $Mn_{0.8}{}^{2+}\ Fe_{0.2}{}^{3+}\ [Mn_{0.2}{}^{2+}Fe_{1.8}{}^{3+}]\ O_4{}^{2-}$. The cation distribution in the spinel structure leads to the exchange interaction between the sublattices A and B, which increases the magnetization of the $MnFe_2O_4$ nanoparticles. The extremely interesting size-dependent optical and electronic properties of II–VI semiconductors have attracted great attention from researchers.[33,34] Among these, ZnS has exciting optical properties such as high photostability, size-dependent chemical stability, electrical properties caused by quantum size effect, and high luminescence efficiency. Besides, ZnS host diluted magnetic semiconductor (DMS) motivates the scientists worldwide due to their exchange interaction between the spins of carrier host semiconductors and dopant atoms that provide the ferromagnetic order in the whole lattice at room temperature.[35–38] Multifunctional magnetic-fluorescent nanocomposites are very propitious materials for biomedical applications. In our previous study, we have reported that the heat generation is stimulated by the ZnS concentration on $MnFe_2O_4$/ZnS nanocomposite.[39] There are various challenges associated with the fabrication of these types of nanocomposites. Direct contact between the two entity yield the possibility of quenching fluorophore on the surface of the nanoparticles. Again, quenching may also happen between the fluorescence molecules attached to the magnetic nanoparticles.[40] To address this issue, a suitable combination of biomolecules with magnetic nanoparticles before the introduction of the quantum dot is highly essential. The introduction of biomolecules also increases the possibility

Department of Physics, National Institute of Technology Nagaland, Chumukedima, 797103, India. E-mail: jpborah@rediffmail.com

of biomolecule recognition[41] and magnetic field-assisted drug delivery.[42] Yang Xu *et al.* reported Fe_3O_4/SiO_2-QDs nanocomposite where SiO_2 acted as a coupling agent. They found that the nanocomposite showed multifunctional superparamagnetic and photoluminescent properties, suitable for *in vivo* hyperthermia.[43] Again Erqun Song *et al.* prepared magnetic-encoded fluorescent $CdTe/Fe_3O_4@SiO_2$ nanospheres using reverse microemulsion method.[44] The nanocomposite showed good fluorescence properties, gradient magnetic susceptibility and easy biofunctionalization for biomolecules. Apart from these, several groups have been reporting various biomolecules to conjugate magnetic and fluorescence counterpart *e.g.* $Fe_3O_4@SiO_2$ nanoparticles and modified the surface using APS (3-aminopropyltrimethoxysilane).[45] Zhang *et al.* also explored a series of platforms for developing multifunctional magnetic/fluorescent nanocarriers loaded with different drugs for cell imaging and treatments.[46,47] The magnificent physico-chemical, transport, bio-degradable, and conjugation properties of dextran have recently fascinated the sizeable interest as an exciting agent of the targeted drug-delivery polymer.[48] The advantage of using Dextran coating is to prevent magnetic nanoparticle aggregation in the blood vessel and act as a coupling agent to bind the magnetic and fluorescent nanoparticle covalently. In this work, we have investigated the magneto-optical properties of Dextran mediated $MnFe_2O_4$/ZnS nanocomposites for efficient control of self-heating properties. We have analyzed the structural, morphological, optical and magnetic properties of the nanocomposites with varying ZnS concentration. Besides, we have also reported the optimized self-heating properties of the nanocomposite with the varying concentration of ZnS for magnetic hyperthermia applications.

2. Experimental section

2.1. Materials

In this paper, we have used $MnCl_2 \cdot 4H_2O$, $FeCl_3$, and NaOH of 2.0 M as precursor materials for synthesizing $MnFe_2O_4$ at room temperature while zinc acetate [Zn $(CH_3COO)_2$] of 0.2 M and sodium sulphide $[Na_2S \cdot 9H_2O]$ of 0.2 M was used as a precursor for synthesizing ZnS. Dextran "$[H(C_6H_{10}O_5)_x$ OH]" was used as a surfactant to modify the surface of $MnFe_2O_4$ nanoparticles.

2.2. Synthesis methods

$MnFe_2O_4$ magnetic nanoparticles and ZnS nanoparticles were synthesized by a simple co-precipitation method as reported by our group.[39]

2.3. Synthesis of $MnFe_2O_4$/Dex

The prepared $MnFe_2O_4$ nanoparticles and Dextran of specific ratios were mixed separately in 25 ml of de-ionized water at a proper stoichiometric ratio and then stirred at 50 °C for 30 min. Subsequently, the mixer sonicates for 90 min at 50 °C and then centrifuged at 3000 r.p.m for 15 min. The resulting black precipitate was washed and dried at 60 °C for 12 hours. After grinding the acquired solid product $MnFe_2O_4$/Dex nanocomposites were obtained.

2.4. Synthesis of $MnFe_2O_4$/Dex@ZnS 1%, 3% and 5%

$MnFe_2O_4$/Dex and ZnS nanoparticles were dissolved separately in 25 ml of de-ionized water at 1% wt. ratio of $MnFe_2O_4$/Dex. Thereafter both the solution were mixed and stirred continuously for 30 min at 50 °C and then sonicated for 90 min at 50 °C. The resulting solution was centrifuged at a rate of 2000 r.p.m for 15 min and then washed four times with de-ionized water. The acquired precipitate was dried for 12 hours at 60 °C and then ground to powder. Thus, the $MnFe_2O_4$/Dex@ZnS 1% nanocomposite was prepared. Similarly, the nanocomposites of 3% and 5% ZnS were also prepared.

3. Characterization

With the help of a powder X-ray diffractometer (Rigaku, RINT 2500 TRAX-III), the XRD spectra of the samples were characterized by using Cuk_α radiation of wavelength $\lambda = 1.5406$ Å. The morphology of the synthesized materials was analyzed by a high resolution transmission electron microscope (JEOL. Model. JEM 2100). A Cary 630 Fourier transform infrared (FT-IR) (Agilent Technology) was employed to study the vibrational spectra of synthesized samples. The investigation of Photoluminescence (PL) spectra of synthesized samples was done by the fluorescence spectrometer [Thermospectronic AMINCO Bowman (series 2)]. A Vibrating Sample Magnetometer (VSM) (Model: 7410 series) was utilized to explore the various magnetic parameters of the samples.

3.1. Induction heating

The induction heating efficiency of various samples with diverse concentrations was investigated at the hand of Easy Heat 8310, Ambrell, UK having a coil of 8 turns. All the sample of mass 2 mg was draped in 1 ml of distilled water, then sonicated for 15 min for relevant suspension, after that it was placed at the centre of the water-cooled induction coil. The AC magnetic field of frequency 336 kHz was fixed and the values of current were kept constant at 250 A and 350 A. The amplitude of the magnetic field was calculated using the relation

$$H = NIa^2 \Big/ 2\sqrt[3]{z^2 + a^2} \quad (1)$$

where N represents the number of turns in the induction coil, z is the distance from the centre of the coil on the z-axis, 'a' is the radius of the coil and I is the current.

4. Result and discussion

4.1. Structural and morphological studies

Fig. 1(ii) shows the XRD pattern of Dextran coated $MnFe_2O_4$/ZnS nanocomposites with various concentrations of ZnS (1%, 3%, and 5%). For clarity and comparison purpose, we have also displayed the XRD spectra of bulk $MnFe_2O_4$, ZnS and Dextran coated $MnFe_2O_4$ nanoparticle in Fig. 1i[a–c]. The spectra illustrating the peaks of pure $MnFe_2O_4$ corresponds to the reflection planes (311), (331), (511),(440) and (531), which matches with the standard XRD pattern (JCPDS 73-1964) and confirms the

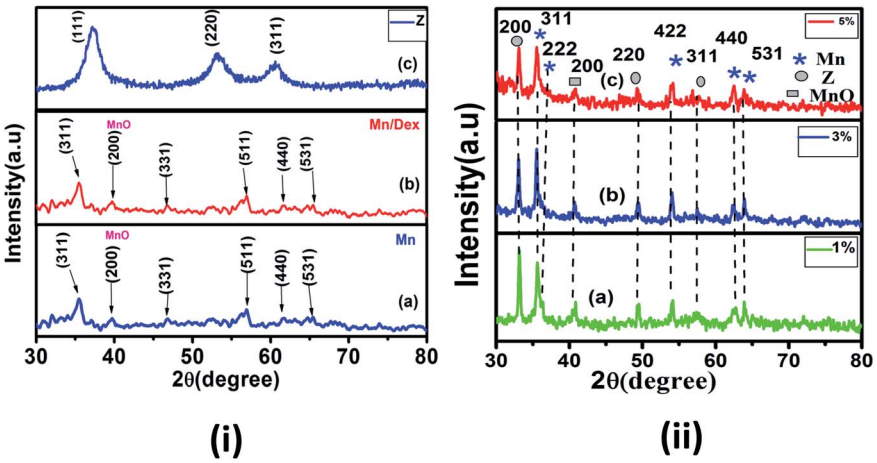

Fig. 1 X-ray pattern of (i) (a) pure Mn ($MnFe_2O_4$) (b) Mn/Dex (c) pure Z(ZnS) and (ii) Mn with Z (a) 1% (b) 3% and (c) 5% nanocomposite.

existence of the cubic spinel phase of $MnFe_2O_4$ in all the nanocomposites. On the other hand, the diffraction peaks corresponding to the lattice planes (200), (220), and (311) signify the presence of the cubic zinc blend phase of ZnS (JCPDS 80-0020). An impurity peak ($2\theta \sim 40^\circ$) due to MnO is observed in the spectra due to the impurities present in the precursor materials used in the synthesis process. Therefore, the existence of both the cubical phases of spinel $MnFe_2O_4$ and the cubical zinc blend phase of ZnS in the coated nanocomposite is confirmed from the XRD study. To obtain accurate crystallite size and microstrain of the samples, we have adopted three methods. In Williamson and hall method[49] or uniform deformation model (UDM), the crystallite sizes were calculated by considering the uniform strain on each of the crystallographic planes. It is good to represent non-uniform strain in all the crystallographic planes. Therefore, to consider the non-uniform strain, the Williamson and hall equation[50] is further modified in terms of stress and Young's modulus as follows

$$\beta \cos\theta = \frac{k\lambda}{D} + \frac{4\sigma \sin\theta}{Y_{hkl}} \quad (2)$$

where 'Y' is Young's modulus of the material. This equation is known as the uniform stress deformation model (USDM). The value of strain (σ) can be determined from the calculated value of Y_{hkl} for every diffracted plane.[51,52] Besides, strain energy density (u) can also be enumerated by further resolving the eqn (2) which is also known as the uniform deformation energy density model (UDEDM) and it is given by

$$\beta \cos\theta = \frac{k\lambda}{D} + 4 \sin\theta \sqrt{\frac{2u}{Y_{hkl}}} \quad (3)$$

The value of strain energy density and crystallite size can be evaluated by plotting $\beta \cos\theta$ against $4 \sin\theta\ (2u/Y_{hkl})^{1/2}$. The slope of the graph gives the value of energy density (u) and the intercept gives the value of crystallite size (D) of the samples. The values of lattice strain can be measured by calculating Y_{hkl} for each diffraction plane and the values of energy density(u) obtained from Hook's energy density relation $u = \varepsilon^2 Y_{hkl}/2$, where ε is the lattice strain. The calculated crystallite size, strain, stress, and strain energy density from each of the model are tabulated in Table 1.

It is noticed that the crystallite size variations of the nanoparticles in all the three methods approximately follow a similar trend. Perceiving the Table 1, it is noted that, the crystallite sizes of the $MnFe_2O_4$ nanoparticles increases from 15.79 nm to 33.3 nm after functionalization with Dextran. The increase in the crystallite size of the magnetic nanoparticles can be attributed to the high binding affinity of dextran molecules with the surface of the nanoparticles which provides the stability to the crystals for further growth. The organic molecules of the

Table 1 Illustrates the structural parameters of $MnFe_2O_4$/ZnS nanocomposites

Sample name	UDM $\varepsilon \times 10^{-4}$	D (nm) (strain)	USDM $\sigma \times 10^{-4}$	$\varepsilon \times 10^{-4}$	D (nm) (TPa)	UDEDM $u \times 10^{-4}$	$\varepsilon \times 10^{-2}$	D (nm)	a (Å)	I_{422}/I_{222}
Z	8.88	4.47	0.423	0.004	4.38	1.33	0.17	4.42	5.3448	
Z (1%)	10.00	38.62	−4.14	−0.05	9.87	−5.89	−0.38	13.50	5.3449	
Z (3%)	9.39	43.46	−2.66	−0.04	13.14	−1.79	−0.19	22.5	5.3450	
Z (5%)	16.0	45.01	3.82	0.01	45.60	5.57	0.22	45.31	5.3458	
Mn	−5.98	15.79	0.598	0.002	19.12	−0.545	−0.06	17.33	8.5084	1.82
Mn/Dex	2.30	33.32	0.947	0.004	36.01	1.09	0.09	34.66	8.5108	
Mn (1%)	−23.0	20.35	−6.07	−0.03	18.63	−8.30	−0.27	19.47	8.5077	1.44
Mn (3%)	−21.0	18.96	−5.24	−0.02	18.38	−7.48	−0.25	18.68	8.5064	1.68
Mn (5%)	−32.0	15.70	−4.49	−0.06	10.13	−0.10	−0.57	10.51	8.5058	1.58

surfactant produce a steric effect at the interface of the nanoparticles which disturbs the effective particle to particle contact and reduces the Brownian motion of the nanoparticles.[53] Diversely the crystallite sizes of the $MnFe_2O_4$ nanoparticles decreases in $MnFe_2O_4$/ZnS nanocomposites when ZnS nanoparticles are incorporated on the surface of the $MnFe_2O_4$ nanoparticles which can be accredited as the conversion of the morphology of irregular shape of synthesized nanoparticles into regular nanospheres. This is consistent with the result obtained by Kavas *et al.*[54] Subsequently, as the concentration of ZnS in the nanocomposites increases the crystallite size of the $MnFe_2O_4$ nanoparticles decreases gradually. The replacement of a greater ionic radius of Mn^{2+} (0.083 nm) ions by a lower ionic radius of Zn^{2+} (0.074 nm) ions may be the possible cause of decreasing crystallite size and lattice constant of $MnFe_2O_4$ nanoparticles.[55,56] On the other hand, the crystallite sizes of the ZnS nanoparticles increases as its concentration in the nanocomposites increases, which can be signified as the huge nucleation growth of ZnS nanoparticles on the surface of the $MnFe_2O_4$ nanoparticles and multiple interfacial strains may also be the possible cause for increasing crystallite sizes of the ZnS nanoparticles. It is well known that Bragg's diffraction peak intensities for (222) and (400) plans are sensitive with the cations in octahedral sites whereas (220) and (422) planes are sensitive to cations in tetrahedral sites.[57] The variation of peak intensity (I_{220}/I_{400}) for all the samples is tabulated in Table 1; it can be speculated that the movement of cations from octahedral to tetrahedral sites increases as the concentration of ZnS increases. The morphology of the samples was investigated by the high-resolution transmission electron microscope. Fig. 2 illustrates the HRTEM images of $MnFe_2O_4$/ZnS nanocomposites with 1%, 3% and 5% ZnS. The micrograph shows the quasi-spherical shape of $MnFe_2O_4$ nanoparticles and the spherical shape of ZnS nanoparticles. The average particle size of $MnFe_2O_4$ nanoparticles ranges from ~15–21 nm and that of ZnS nanoparticles is found to be ~14–45 nm which is consistent with the XRD result. The SAED pattern of 1%, 3% and 5% of ZnS nanocomposites corresponds to the reflection from crystal planes (311), (422), (440), (331) of $MnFe_2O_4$, and (200), (111), (311) of cubic zinc blend structure of ZnS which matches well with the XRD diffractograms result (inset of Fig. 2(a)–(c)). Fig. 2(d) represents the *d*-spacing of (311) planes of $MnFe_2O_4$ and (200) planes of ZnS nanoparticles. Fig. 3 shows the EDAX spectrum of the 3% ZnS nanocomposites with the stoichiometric ratios of unalike components in the nanocomposites and the inset indexed the weight% of contrasting elements in the nanocomposites.

4.2. FTIR analysis

FTIR spectroscopy results of $MnFe_2O_4$ and $MnFe_2O_4$/Dex nanocomposites have been depicted in Fig. 4(a). The peak observed at 440 cm^{-1} and 645 cm^{-1} is the characteristic vibration of Fe–O and Mn–O bond at octahedral (B) sites and tetrahedral (A) sites of spinel ferrite respectively. The peak at 1635 cm^{-1} represents the strong C=O stretching which is also consistent with the result obtained by Ali Amiri *et al.*[58] The absorption peak recorded at 2126 cm^{-1} attributed to weak C≡C stretching and the peak observed at 1025 cm^{-1} is ascribed as the C–O stretching of the ester group of dextran gives the strong evidence of conjugation of dextran on the surface of $MnFe_2O_4$ nanoparticles.[59] Moreover, the absorption peak observed at

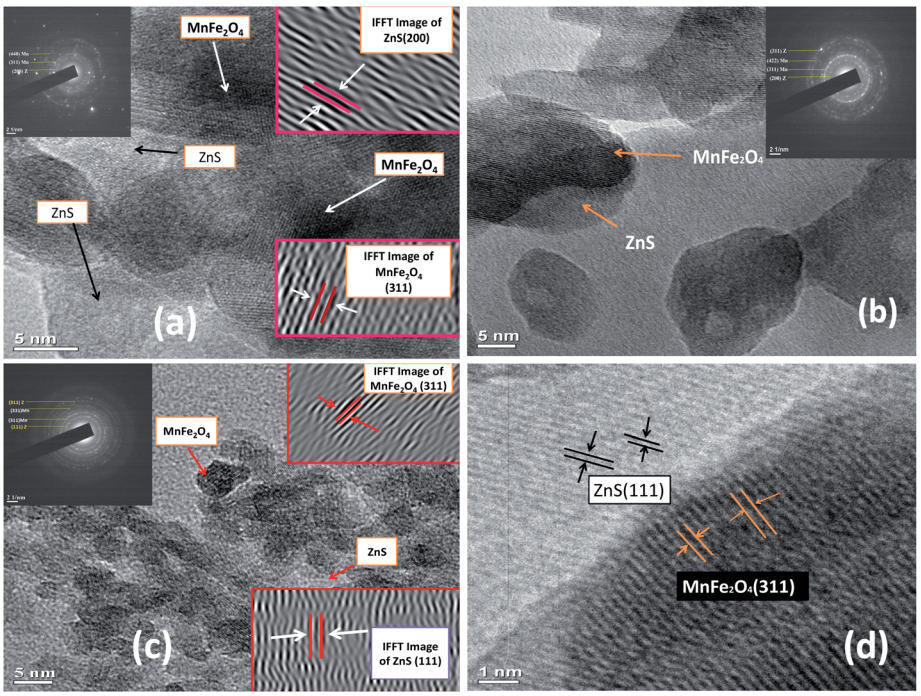

Fig. 2 HRTEM image of $MnFe_2O_4$/ZnS nanocomposites with (a) 1% (b) 3% (c) 5% ZnS and inset depicts their SAED pattern (d) *d*-spacing of (311) plane of $MnFe_2O_4$ and (200) plane of ZnS in the 3% nanocomposites.

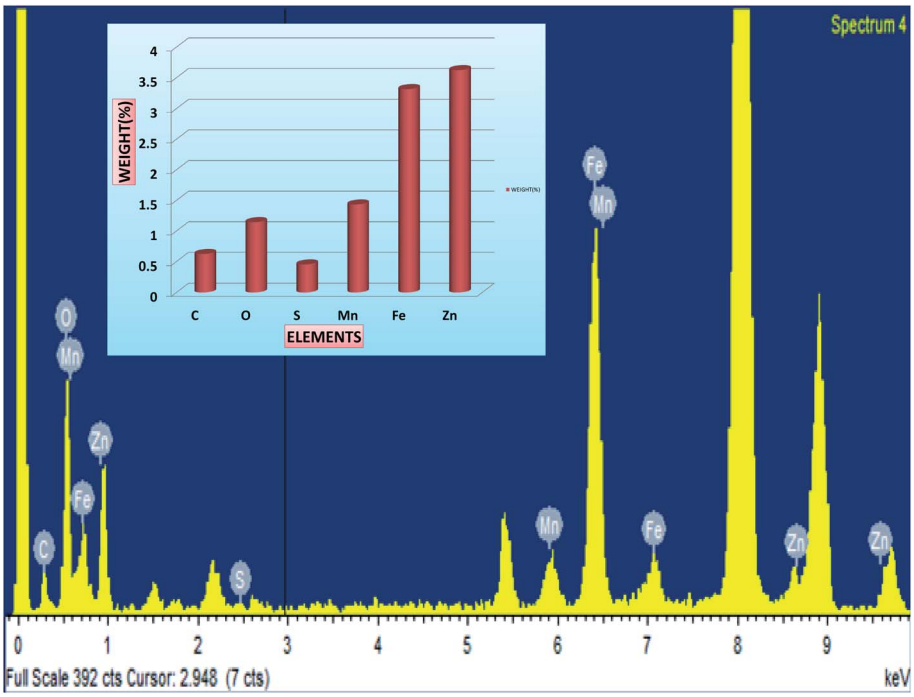

Fig. 3 Presents the EDAX pattern of $MnFe_2O_4$/ZnS nanocomposites with 3% concentration of ZnS and the inset shows the weight% of different elements in the nanocomposites.

around 1430 cm^{-1} in Fig. 4(b) signifies the C–H bending vibration of the alkyl group in ZnS. The broad absorption peak at 3286 cm^{-1} represents the –OH group vibration which signifies the absorption of water molecules on the surface of the nanoparticles. The shifting of peak position from 1637 cm^{-1} ($MnFe_2O_4$/Dex spectra) to 1645 cm^{-1} in the nanocomposites confirms the assimilation of ZnS nanoparticles on the surface of $MnFe_2O_4$/Dex nanocomposites. The schematic diagram of the formation of $MnFe_2O_4$/Dex/ZnS nanocomposite is depicted in Fig. 5.

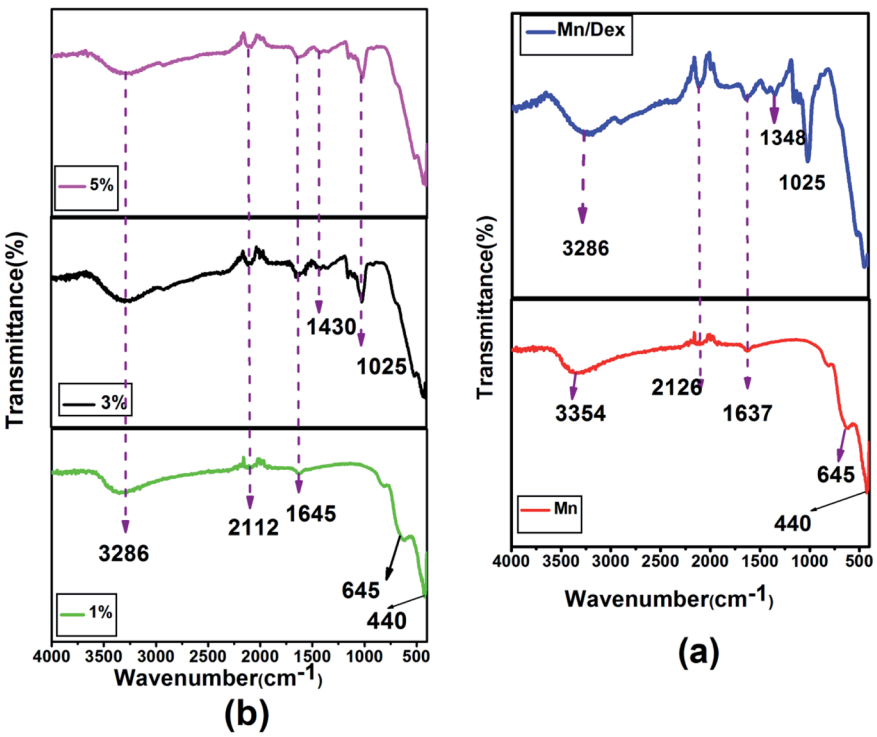

Fig. 4 FTIR spectra of (a) $MnFe_2O_4$ and $MnFe_2O_4$/Dex nanocomposites (b) $MnFe_2O_4$/ZnS nanocomposites with different concentration of ZnS (1%, 3% and 5%).

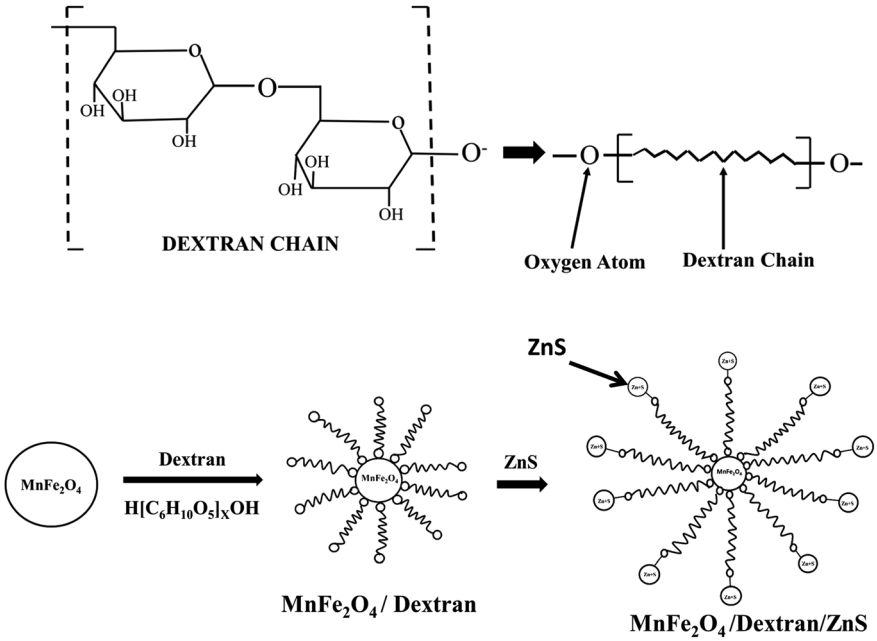

Fig. 5 Schematic diagram of dextran chain and mechanism of the formation of $MnFe_2O_4$/ZnS nanocomposite.

4.3. Photoluminescence studies

The photoluminescence (PL) property of pristine ZnS is differing when their surface chemistry changes after synthesizing nanocomposites with $MnFe_2O_4$/Dextran. PL measurement of the nanocomposite was carried out at room temperature with 260 nm excitation. The entire nanocomposite exhibits multipeak emission which is observed in Fig. 6(a–d). A multipeak Gaussian fit of the nanocomposites with different concentration of ZnS (1%, 3%, and 5%) gives four emission bands located at 279, 292, 311, and 350 nm (Fig. 6(b), (c) and (d)) respectively. The emission peak centres from 279 nm to 311 nm ascribed as the band to band transition in ZnS nanoparticle.[60,61] The peak observed at 350 nm is attributed due to the interstitial sulfur vacancies.[62] The deconvoluted peak shifted from 286 nm to higher wavelength of 292 nm and from 299 to 307 and 311 nm. Fig. 6[(a)–(c)] shows the redshift in the spectrum, which represents the increase in crystallite size of ZnS nanoparticles as the concentration of ZnS increases in

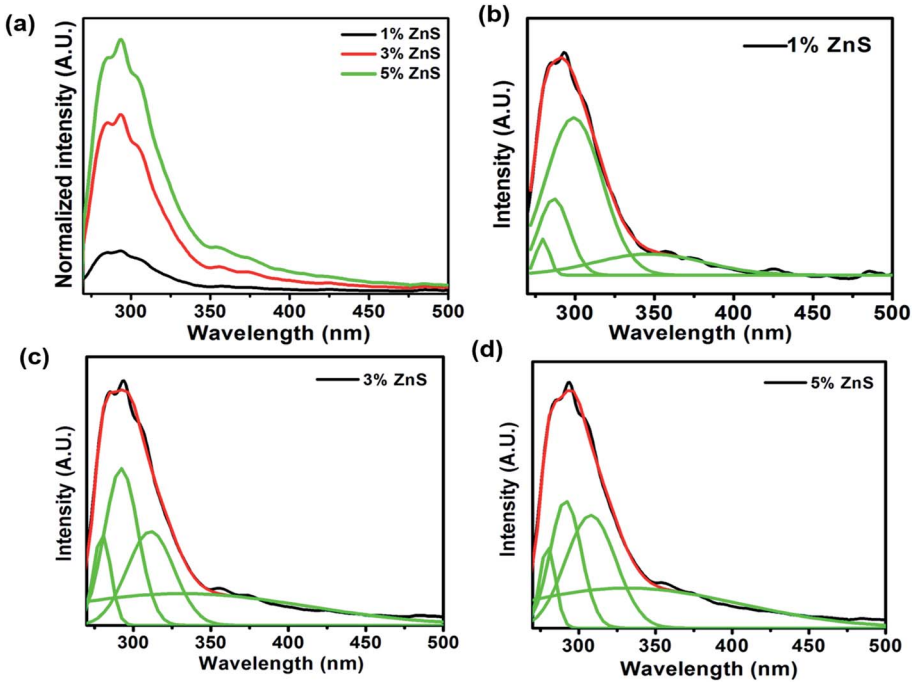

Fig. 6 (a) PL emission spectrums of $MnFe_2O_4$/ZnS nanocomposites with discrete concentration of ZnS and multiple Gaussians fit of (b) 1% (c) 3% and (d) 5% ZnS in the nanocomposite.

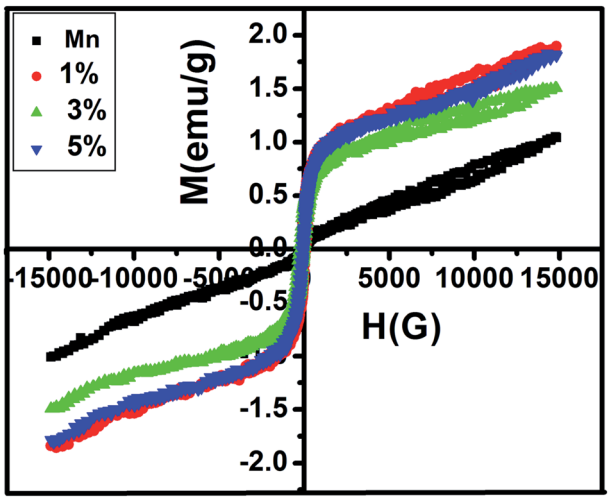

Fig. 7 M–H curve of $MnFe_2O_4$ and $MnFe_2O_4$/ZnS nanocomposites with 1%, 3%, 5% concentration of ZnS.

the $MnFe_2O_4$/ZnS nanocomposites and it is consistent with our XRD result. Alternately, quantum yields of the samples also increase with the increasing crystallite sizes of the ZnS nanoparticles due to the radiative trapping process in the ZnS nanocrystals.[63] In our previous work, we have found that the peaks centred around 303, 328, 351, and 368 nm in the $MnFe_2O_4$ nanocomposites in presence of surfactant PEG.[39] In this work, we observed that most of the intense peaks are in the lower wavelength region whereas in previous work most intense peaks were found in the higher wavelength region, and their intensities were also higher than this work. Therefore, the results indicate that the nanocomposites are still carrying fluorescence, despite quenching by the magnetic counterpart.

4.4. Magnetic analysis

Fig. 7 illustrates the variation of magnetic properties of pure $MnFe_2O_4$ and $MnFe_2O_4$/ZnS nanocomposites with different concentrations of ZnS at room temperature. The magnetic parameters of all the samples are listed in Table 2. The magnetic saturation value of pristine $MnFe_2O_4$ is recorded as 1.0295 emu g^{-1} which is lower than the bulk $MnFe_2O_4$ (80.00 emu g^{-1}). The large spin disorder of the surface nanoparticles may be the possible cause of the decrease of saturation magnetization of synthesized $MnFe_2O_4$ nanoparticles which is similar to the result reported by Kolhatkar *et al.*[64] When the ZnS nanoparticles were incorporated on the active surface of the pure $MnFe_2O_4$ nanoparticles, the magnetic saturation (M_s) value of the nanocomposites significantly increases. The formation of covalent bonds of dextran with the magnetic nanoparticles decreases the surface spin disorder of the nanoparticles which expedited the increase of the M_s value of the nanoparticles.[65] Saturation magnetization is calculated by the fitting of the law of approach.[66] The maximum value of magnetic saturation (M_s) is recorded as 1.87 emu g^{-1} for the sample 1% but as the concentration of ZnS in the nanocomposites increases M_s value of the composites decreases a little. It is well known that in mixed spinel ferrite, tetrahedral site (A) and octahedral site (B) are antiferromagnetically coupled with each other. Thus, when ZnS nanoparticles are added with the $MnFe_2O_4$ nanoparticles, Fe^{3+} ions migrated from A to B site which leads to the increase in the magnetization. Thus the net magnetization of the $MnFe_2O_4$/ZnS increases than the pure $MnFe_2O_4$ nanoparticles.[67,68] The increased concentration of ZnS decreases the number of Mn^{2+} ions in the B site and Fe^{3+} ions in the A site which weakens the role of A–B exchange interactions and strengthens the role of B–B interactions. Due to this, the magnetic moments of Fe^{3+} ions in the B site starts reversibly oriented; as a result, the net magnetization of the spinel ferrite decreases.[69] But due to the more tendencies of occupancy of Mn^{2+} in tetrahedral A site and the corresponding migration of iron ions to the octahedral site, an unexpected increases of saturation magnetization occurs in the sample 5% compared to 3%. This fluctuation of saturation magnetizations in the samples is corroborated with the cation distribution ratio in XRD analysis. As reported in Table 2, the coercivity (H_c) value first increases and then decreases with the crystallite size of the $MnFe_2O_4$ nanoparticles. The increasing crystallite size of the nanoparticles up to the single domain regime and the random orientation of lattice planes may be the leading reasons for enhancement of the H_c value of the nanoparticles.[70,71] The trend of coercivity tuning of the nanocomposites can also be explained from the single-ion anisotropy model. Since Mn^{2+} exhibits a high spin ligand state, B site ions in the structure contribute to magnetocrystalline anisotropy and coercivity through L–S coupling. When ZnS is introduced in the nanocomposite, this accelerated the migration of Mn^{2+} from A site to B site which may be considered as the potential source of the increase in the magnetic anisotropy as well as the coercivity of the nanoparticles.[72] As the concentration of ZnS increases further, the concentration of Mn^{2+} ion in the octahedral site decreases owing to less anisotropy environment at the tetrahedral sites and leads to a decrease in coercivity.

Table 2 Represents the variation of magnetic parameters of $MnFe_2O_4$/ZnS nanocomposites with the concentration of ZnS

Sample name	Coercivity (H_c) (G)	Saturation magnetization (M_s) (emu g^{-1})	Remanence (M_r) (emu g^{-1})
$MnFe_2O_4$	14.185	1.0295	0.02569
ZnS-1%	115.28	1.8774	0.26044
ZnS-3%	108.42	1.5009	0.20042
ZnS-5%	103.71	1.8182	0.232

4.5. Induction heating curve analysis

The generation of heat by magnetic nanoparticles, when exposed to the AC magnetic field of suitable frequency for hyperthermia application, can be elucidated with the fluctuation of temperature as a function of time. Fig. 8 shows the variation of temperature with time measured for the samples of pure $MnFe_2O_4$ and $MnFe_2O_4$@ZnS nanocomposite (1%, 3%, and 5% ZnS) at different sample concentrations (frequency 336

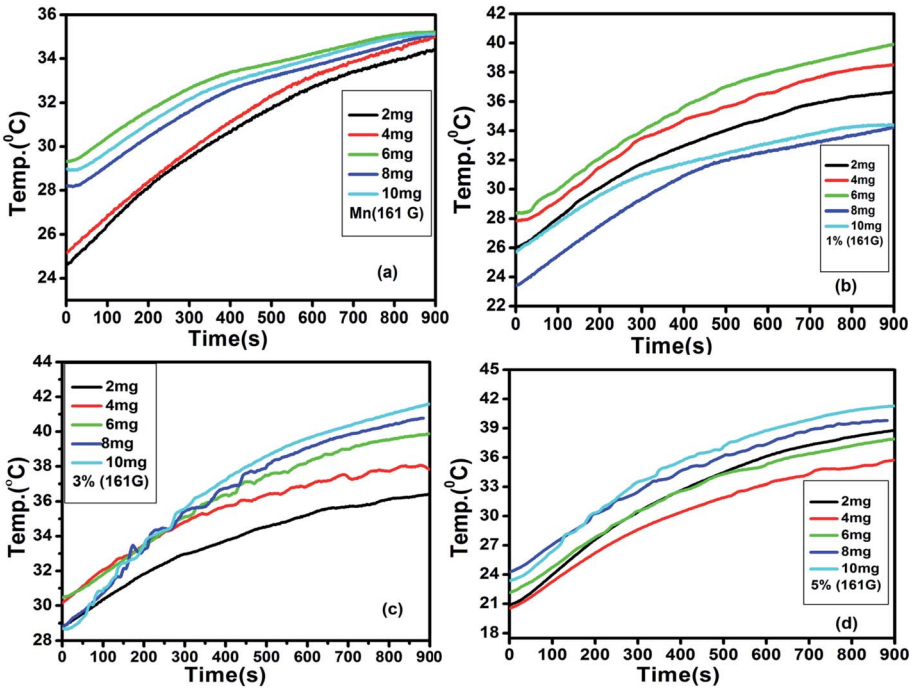

Fig. 8 Induction heating curves of (a) Mn (b) 1% (c) 3% (d) 5% (ZnS) with concentration (2, 4, 6, 8 and 10 mg ml^{-1}) at frequency 336 kHz, current 250 A and AC magnetic field amplitude $H = 161$ G.

kHz and the magnetic field amplitude of 161 G). The alteration of temperature with time for all the samples was recorded for 15 min. Looking at the figure, it is apparent that as the sample concentration increases the maximum temperature attained by the sample also increases. It is perceived from Fig. 8(c) that the sample 3% ZnS (with a concentration of 10 mg ml^{-1}) attains a maximum temperature of 41.67 °C which is just ~4 °C less than the critical temperature (45.67 °C) for efficient hyperthermic application.[73] Throughout the experiment, a safety limit of C=H. $f = 6 \times 10^9$ A m^{-1} s^{-1} has been set for all the

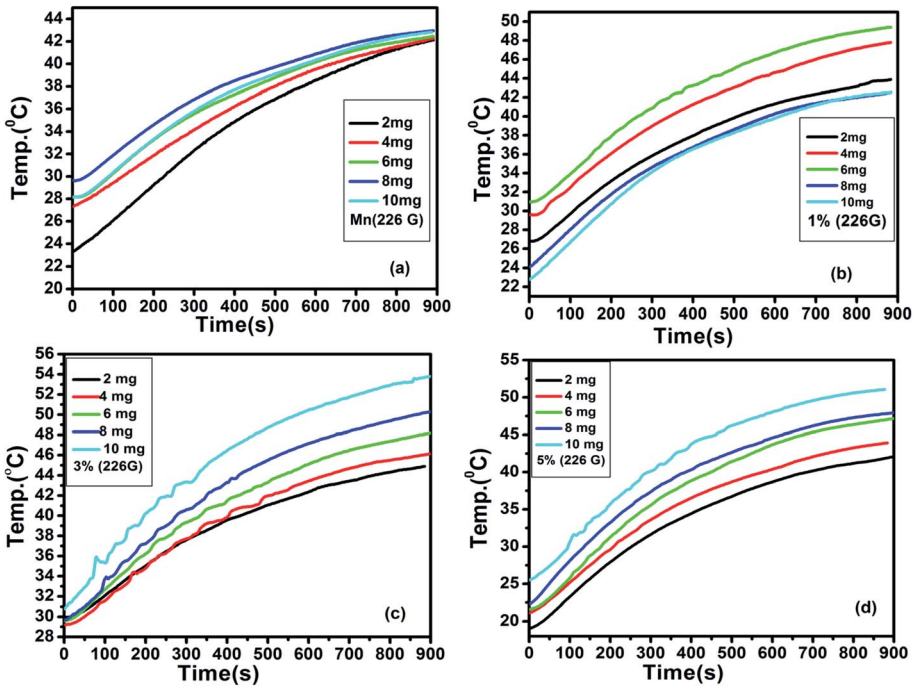

Fig. 9 Induction heating curves of (a) Mn (b) 1 (c) 3% (d) 5% (ZnS) with concentration (2, 4, 6, 8 and 10 mg ml^{-1}) at frequency 336 kHz, current 350 A and AC magnetic field amplitude $H = 226$ G.

samples as suggested by Hergt.[74] Therefore it is speculated that at field amplitude $H = 161$ G, all the samples show a lower saturation temperature than the competent hyperthermia threshold temperature. In our investigation, we experienced some fluctuation in heating curves for some samples, which can be ascribed as the erratic particle size distribution. In the presence of an external AC magnetic field, with the increase in the time interval of the magnetic nanoparticles, there is an elevation of surrounding temperature which results in the reduction of the magnetic moment of $MnFe_2O_4$ nanoparticles. In such a circumstance the fluctuation in the temperature variation curve is relevant. Seongate Bae *et al.* also observed a similar result for $NiFe_2O_4$ nanoparticles.[75] Again, we have analyzed the time–temperature variation with higher magnetic field amplitude $H = 226$ G for all the samples as depicted in Fig. 9.

It was observed that with the increase in field amplitude all the samples reached threshold hyperthermic temperature ~45 °C (Fig. 9). The heating efficiency of the magnetic nanoparticles can be measured as the specific absorption rate (SAR) or specific loss power (SLP) and is calculated by employing the phenomenological Box Lucas equation.[76]

$$T - T_0 = \frac{P}{L}\left(1 - e^{\frac{(t-t_0)L}{C}}\right) \quad (4)$$

where P is the power dissipated by the magnetic nanoparticles, C is the specific heat of solvent (measure in J K^{-1}), $(T - T_0)$ is the temperature difference between the medium and surrounding materials, t_0 is the parameter generally used for the correction of the non-zero start of the curve and L (measure in W K^{-1}) is a constant that quantifies the proportionality between the temperature and losses. The experimental heating curved were non-linearly fitted with Box Lucas equation (Fig. 10) and the SAR values were evaluated using the equation

$$\mathrm{SAR} = \frac{M_s}{M_n} \times C\ (a\ \times b) \quad (5)$$

where M_s is the mass of suspension and M_n is the magnetic nanoparticles in suspension, on the other hand, '*a*' and '*b*' represents the fitting constants. To compare the heating efficiency of the magnetic nanoparticles, we have introduced another parameter, known as intrinsic loss power (ILP). The value of intrinsic loss power can be obtained from the following equation.[77]

$$\mathrm{ILP} = \frac{\mathrm{SAR}}{fH^2} \quad (6)$$

where SAR is measured in W g^{-1}, f is the frequency (in kHz) and H is the amplitude (kA m^{-1}) of the AC magnetic field respectively. The estimated SAR and ILP values are tabulated in Tables 3 and 4 respectively.

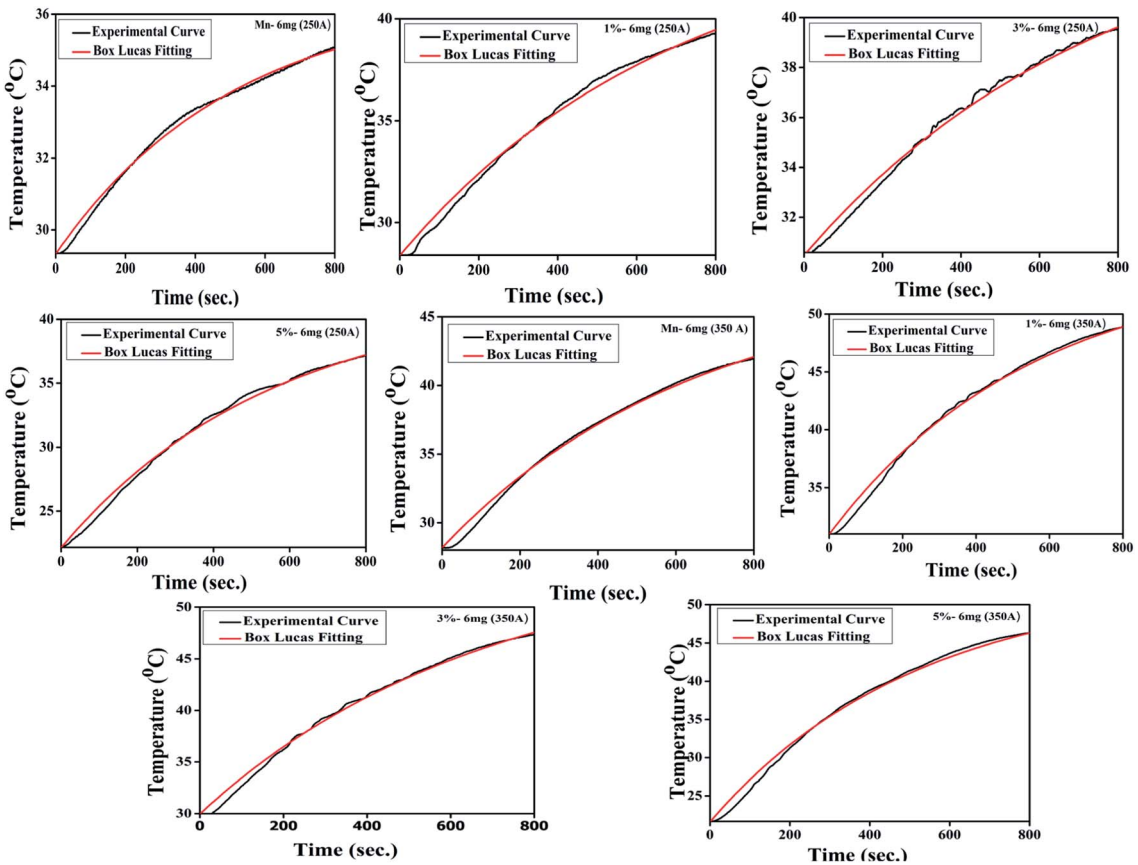

Fig. 10 The representative Box Lucas Fitting for induction heating curve (concentration 6 mg) of each sample.

Table 3 Depicts the calculated SAR values of pure $MnFe_2O_4$ and $MnFe_2O_4$/ZnS nanocomposites with different concentration of ZnS

	SAR value for different samples at $H = 161$ G				SAR value for different samples at $H = 226$ G			
Amount	Mn (W g^{-1})	1% (W g^{-1})	3% (W g^{-1})	5% (W g^{-1})	Mn (W g^{-1})	1% (W g^{-1})	3% (W g^{-1})	5% (W g^{-1})
2 mg	12.54	50.94	37.70	52.67	27.06	81.19	64.83	115.62
4 mg	10.78	22.72	22.52	36.84	24.32	40.92	36.37	55.58
6 mg	9.86	16.17	18.96	24.96	21.05	29.80	29.96	42.55
8 mg	7.16	14.71	14.36	18.11	15.86	26.24	24.57	36.45
10 mg	5.24	12.82	12.46	18.04	14.83	22.34	21.00	27.03

Table 4 Shows the calculated ILP values of pristine $MnFe_2O_4$ and $MnFe_2O_4$/ZnS nanocomposites with various concentration of ZnS

	ILP values of different samples at $H = 161$ G				ILP values of different samples at $H = 226$ G			
Amount	Mn (nHm^2 kg^{-1})	1% (nHm^2 kg^{-1})	3% (nHm^2 kg^{-1})	5% (nHm^2 kg^{-1})	Mn (nHm^2 kg^{-1})	1% (nHm^2 kg^{-1})	3% (nHm^2 kg^{-1})	5% (nHm^2 kg^{-1})
2 mg	0.22	0.89	0.66	0.92	0.25	0.74	0.59	1.06
4 mg	0.19	0.40	0.39	0.64	0.22	0.37	0.33	0.51
6 mg	0.17	0.28	0.33	0.43	0.19	0.27	0.27	0.39
8 mg	0.13	0.25	0.25	0.32	0.15	0.24	0.22	0.34
10 mg	0.092	0.21	0.22	0.30	0.13	0.21	0.19	0.24

It is well known that when the size of the magnetic nanoparticles reduces to a critical size regime or transits to a single domain, thermal fluctuation becomes comparable to the energy barrier. During the Brownian relaxation process the thermal energy is delivered through shear stress in the surrounding fluid (viscous heating) and during the Neel relaxation process, the heat energy is dissipated by the rearrangement of atomic dipole moments within the crystal.[78] The thermal energy is released due to an AC magnetic field which derives the moment of the magnetic nanoparticles from its preferred orientation and the relaxation of the magnetic moments of the nanoparticles back to the equilibrium state, such a process results in local heating.[79] It is noteworthy that the obtained values of SAR and ILP decrease gradually with the raising concentration (Fig. 11 and 12) of the magnetic nanoparticles. The dipole interaction substantially affects the magnetic behaviour like the magnetic relaxation time[80,81] susceptibility, remanence, coercivity, and blocking temperature[82] of the nanoparticles, which leads to the modification of the self-heating efficiency.[83] As the concentration of magnetic nanoparticles increases, the dipolar interaction also increases owing to the decrease in the interparticle distance, changing the magnetic response of the whole dispersed liquid as well as increases the anisotropic barrier of the nanoparticles, which may be the possible reason for the decreasing SAR values of the samples.[84] According to Ruta *et al.*[85] SAR value changes following the magnetic saturation of

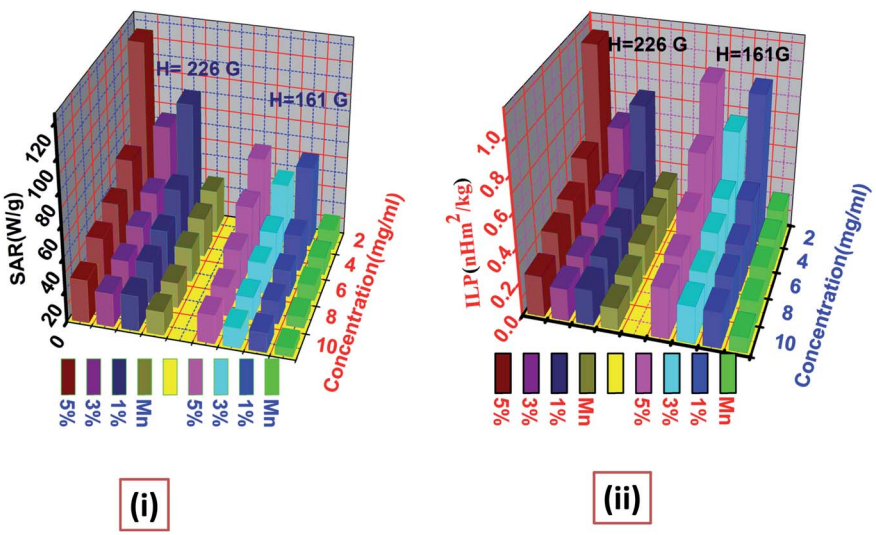

Fig. 11 Illustrates the variation of (i) SAR and (ii) ILP values with different concentration for AC magnetic field of amplitude $H = 161$ G and $H = 226$ G.

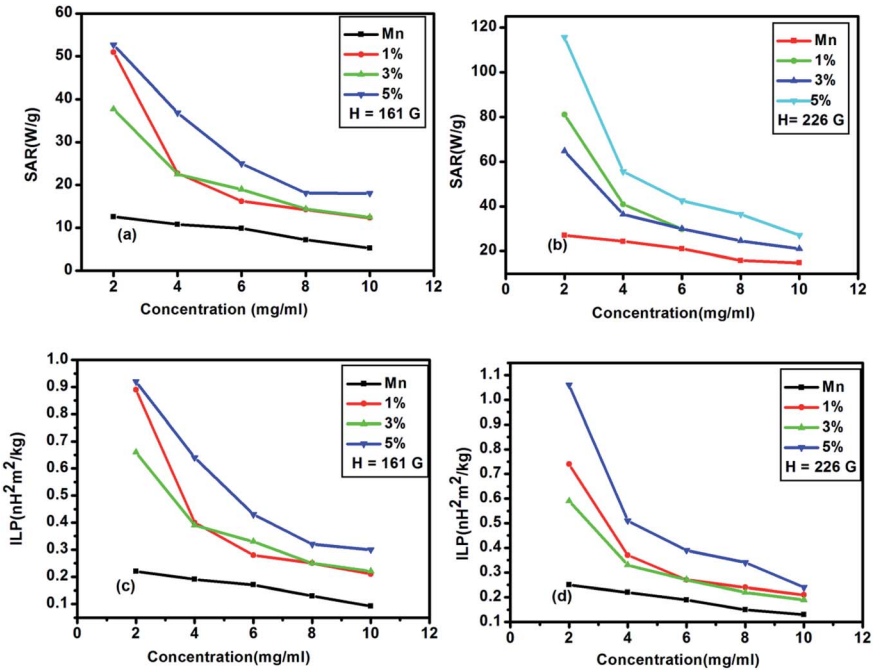

Fig. 12 (a), (b) shows variation of SAR values and (c), (d) depicts the fluctuation of ILP values with different concentrations for AC magnetic field amplitude $H = 161$ G and $H = 226$ G.

the samples because SAR value is directly proportional to AC susceptibility, On the other hand, AC susceptibility changes with M_s value as $\chi_0 = \frac{\mu_0}{3}\frac{VmM_s{}^2}{\phi K_B T}$,[86] which is congruous with our magnetic analysis result. Interestingly, we have found that the SAR value increases for the same concentration in all the samples when the amplitude of the magnetic field increases. Since SAR value directly depends on the amplitude of the AC magnetic field such as SAR $\cong kf^nH^2$.[87] Where k is the material constant based on frequency, f is the frequency of magnetic field, n is a constant of numeric value 1 for non-superparamagnetic nanoparticles and H is the amplitude of the applied magnetic field. Thus, the increase of SAR value with the increase in the value of H can ascribe to the increasing amplitude of the magnetic field. Hence, such behaviour demonstrates that the heating efficiency of the nanoparticle can be precisely controlled through the AC magnetic field amplitude. This dependence could also be related to the shifting of domain walls as suggested by linear response theory (LRT).[88]

5. Conclusion

In summary, we have developed $MnFe_2O_4$/ZnS magnetic fluorescent nanocomposite by integrating two unique types of nanomaterials, $MnFe_2O_4$ and ZnS semiconductor QDs mediated by Dextran through simple co-precipitation technique. The XRD spectrum illustrates the presence of both the cubical phase of spinel $MnFe_2O_4$ and the cubical zinc blend phase of ZnS in the nanocomposites. The average crystallite size of $MnFe_2O_4$ nanoparticles was recorded as 15–21 nm and 40–45 nm for ZnS nanoparticles in the nanocomposites. In the FTIR spectrum, the absorption peak at 1430 cm^{-1} and 1025 cm^{-1} signifies the incorporation of ZnS nanoparticles on the surface of $MnFe_2O_4$ nanoparticles *via* characteristic vibration of C–O stretching of ester group from dextran. The photoluminescence study concludes that the nanocomposite exhibits luminescence properties after the incorporation of the magnetic materials. The luminescent intensity of the nanocomposites increases as the concentration of ZnS increases in the nanocomposites. Magnetic properties of this nanocomposite are largely dependent on ZnS concentration which might be due to the cationic re-arrangement in the mixed spinel structure. The induction heating curve analysis demonstrates that the heating efficiency of the nanocomposites increases as the concentration of ZnS in the nanocomposites increases. Thus, the present work demonstrates that this dextran mediated $MnFe_2O_4$/ZnS nanocomposite is a promising heating agent for magnetic hyperthermia, which can be controlled by tuning the concentration of semiconductor counterpart.

Conflicts of interest

There are no conflicts to declare.

Acknowledgements

The authors would like to thank Central Instrumentation Facility (CIF), Indian Institute of Technology Guwahati for providing avail facilities and would also like to acknowledge Sophisticated Analytical Instrument Facility (SAIF), NEHU University Shillong for helping us access TEM and SEM facilities.

References

1 G. Song, W. Chen, P. Dang, S. Yang, Y. Zhang, Y. Wang, R. Xiao, R. Ma and F. Li, *Nanoscale Res. Lett.*, 2018, **13**, 364.
2 X. Luo, Z. Pan, F. Pei, Z. Jin, K. Miao, P. Yang, H. Qian, Q. Chen and G. Feng, *J. Ind. Eng. Chem.*, 2018, **59**, 410–415.
3 J. Ren, Q. Luo, Q. Hou, H. Chen, T. Liu, H. He, J. Wang, Q. Shao, M. Dong, S. Wu, N. Wang, J. Lin and Z. Guo, *ChemElectroChem*, 2019, **6**, 3167–3174.
4 H. Sun, Z. Yang, Y. Pu, W. Dou, C. Wang, W. Wang, X. Hao, S. Chen, Q. Shao, M. Dong, S. Wu, T. Ding and Z. Guo, *J. Colloid Interface Sci.*, 2019, **547**, 40–49.
5 B. Lin, Z. Lin, S. Chen, M. Yu, W. Li, Q. Gao, M. Dong, Q. Shao, S. Wu, T. Ding and Z. Guo, *Dalton Trans.*, 2019, **48**, 8279–8287.
6 C. Shen, X. Liu, H. Cao, Y. Zhou, J. Liu, J. Tang, X. Guo, H. Huang and X. Chen, *Appl. Sci.*, 2019, **9**, 1708.
7 M. Liu, Y. Liu, Y. Yan, F. Wang, J. Liu and T. Liu, *Chem. Commun.*, 2017, **53**, 9097–9100.
8 P. Yang, L. Yang, Q. Gao, Q. Luo, X. Zhao, X. Mai, Q. Fu, M. Dong, J. Wang, Y. Hao, R. Yang, X. Lai, S. Wu, Q. Shao, T. Ding, J. Lin and Z. Guo, *Chem. Commun.*, 2019, **55**, 9011–9014.
9 H. Gu, X. Xu, J. Cai, S. Wei, H. Wei, H. Liu, D. P. Young, Q. Shao, S. Wu, T. Ding and Z. Guo, *Chem. Commun.*, 2019, **55**, 10068–10071.
10 Y. Ma, C. Hou, H. Zhang, Q. Zhang, H. Liu, S. Wu and Z. Guo, *Electrochim. Acta*, 2019, **315**, 114–123.
11 K. Le, Z. Wang, F. Wang, Q. Wang, Q. Shao, V. Murugadoss, S. Wu, W. Liu, J. Liu, Q. Gao and Z. Guod, *Dalton Trans.*, 2019, **48**, 5193–5202.
12 A. J. Berndt, J. Hwang, M. D. Islam, A. Sihn, A. M. Urbas, Z. Ku and J. E. Ryu, *Polymer*, 2019, **176**, 118–126.
13 G. Zhu, X. Cui, Y. Zhang, S. Chen, M. Dong, H. Liu, Q. Shao, T. Ding, S. Wu and Z. Guo, *Polymer*, 2019, **172**, 415–422.
14 H. Gu, X. Xu, M. Dong, P. Xie, Q. Shao, R. Fan, C. Liu, R. Wei and Z. Guo, *Carbon*, 2019, **147**, 550–558.
15 Z. Lin, B. Lin, Z. Wang, S. Chen, C. Wang, M. Dong, Q. Gao, Q. Shao, T. Ding, H. Liu, S. Wu and Z. Guo, *ChemCatChem*, 2019, **11**, 2217–2222.
16 Y. C. Park, J. Paulsen, R. Nap, R. D. Whitaker, V. Mathiyazhagan, Y. Song, M. Hurlimann, I. Szleifer and J. Y. Wong, *Langmuir*, 2014, **30**, 784–792.
17 A. Cao, R. Lu and G. Veser, *Phys. Chem. Chem. Phys.*, 2010, **12**, 13499–13510.
18 S. Anas, K. V. Mahesh, V. Jobin, S. Prasanth and S. Ananthakumar, *J. Mater. Chem. C*, 2013, **1**, 6455–6462.
19 G. Boulon, G. Alombert-Goget, Y. Guyot, M. Guzik, T. Epicier, N. P. Blanchard, L. Chen, L. Hu and W. Chen, *J. Mater. Chem. C*, 2014, **2**, 9385–9397.
20 Y. Ding, H. Yin, S. Shen, K. Sun and F. Liu, *New J. Chem.*, 2017, **41**, 1736–1743.
21 D. H. Ortgies, L. de la Cueva, B. del Rosal, F. Sanz-Rodríguez, N. Fernández, M. C. Iglesias-de la Cruz, G. Salas, D. Cabrera, F. J. Teran and D. Jaque, *ACS Appl. Mater. Interfaces*, 2016, **8**, 1406–1414.
22 Q. Ma, Y. Nakane, Y. Mori, M. Hasegawa, Y. Yoshioka, T. M. Watanabe, K. Gonda, N. Ohuchi and T. Jin, *Biomaterials*, 2012, **33**, 8486–8494.
23 Q. Zhang, T. Yin, G. Gao, J. G. Shapter, W. E. Lai, P. Huang, W. Qi, J. Song and D. Cui, *Appl. Mater. Interfaces*, 2017, **9**, 17777–17785.
24 M. Lundqvist, J. Stigler, G. Elia, I. Lynch, T. Cedervall and K. A. Dawson, *Proc. Natl. Acad. Sci. U. S. A.*, 2008, **105**, 14265–14270.
25 R. E. Rosensweig, *J. Magn. Magn. Mater.*, 2002, **252**, 370.
26 A. S. Eggeman, S. A. Majetich, D. Farrel and Q. A. Pankhust, *IEEE Trans. Magn.*, 2007, **43**, 2451.
27 C. G. Hadjipanayis, M. J. Bonder, S. Balakrishnan, X. Wang, H. Mao and G. C. Hadjipanayis, *Small*, 2008, **11**, 1925.
28 J. Carrey, B. Mehdaoui and M. Respaud, *J. Appl. Phys.*, 2011, **109**, 083921.
29 J. Lu, S. Ma, J. Sun, C. Xia, C. Liu, Z. Wang, X. Zhao, F. Gao, Q. Gong, B. Song, X. Shuai, H. Ai and Z. Gu, *Biomaterials*, 2009, **30**, 2919.
30 H. Yang, Y. Zhuang, H. Hu, X. Du, C. Zhang, X. Shi, H. Wu and S. Yang, *Adv. Funct. Mater.*, 2010, **20**, 1733.
31 H. Yang, C. Zhang, X. Shi, H. Hu, X. Du, Y. Fang, Y. Ma, H. Wu and S. Yang, *Biomaterials*, 2010, **31**, 3667.
32 Y. Ding, H. Yin, S. Shen, K. Sun and F. Liu, *New J. Chem.*, 2017, **41**, 1736–1743.
33 L. E. Brus, *J. Chem. Phys.*, 1983, **79**, 5566–5571.
34 M. Nirmal and L. E. Brus, *Acc. Chem. Res.*, 1999, **32**(5), 407–414.
35 T. Endres, M. Zheng, A. Kiliç, A. Turowska, M. B. Broichsitter, H. Renz, O. M. Merkel and T. Kissel, *Mol. Pharmaceutics*, 2014, **11**, 1273–1281.
36 W. Moreels, K. Lambert, D. D. Muynck, F. Vanhaecke, D. Poelman, J. C. Martins, J. Allan and Z. Hens, *Chem. Mater.*, 2007, **19**, 6101–6106.
37 G. Murugadoss and V. Ramasamy, *Luminescence*, 2013, **28**, 195–201.
38 M. S. Akhtar, Y. G. Alghamdi, M. A. Malik, R. M. Arif Khalil, S. Riazb and S. Naseemb, *J. Mater. Chem. C*, 2015, **3**, 6755–6763.
39 D. K. Mondal, C. Borgohain, N. Paul and J. P. Borah, *J. Mater. Res. Technol.*, 2019, **8**(6), 5659–5670.
40 S. A. Corr, Y. P. Rakovich and Y. K. Gun'ko, *Nanoscale Res. Lett.*, 2008, **3**, 87–104.
41 D. K. Kim, Y. Zhang, J. Kehr, T. Klason, B. Bjelke and M. J. Muhammed, *Magn. Magn. Mater.*, 2001, **225**, 256.
42 J. Carpenter, *Magn. Magn. Mater.*, 2001, **17**, 225.
43 Y. Xu, A. Karmakar, D. Wang, M. W. Mahmood, F. Watanabe, Y. Zhang, A. Fejleh, P. Fejleh, Z. Li and J. Kannarpady, *J. Phys. Chem. C*, 2010, **114**, 5020–5026.
44 E. Song, W. Han, J. Li, Y. Jiang, D. Cheng, Y. Song, P. Zhang and W. Tan, *Anal. Chem.*, 2014, **86**, 9434–9442.
45 Y. N. Wu, P. Liang and G. Cheng, *Appl. Phys. A*, 2016, **122**, 243.
46 J. M. Shen, X. M. Guan, X. Y. Liu, J. F. Lan, T. Cheng and H. X. Zhang, *Bioconjugate Chem.*, 2012, **23**, 1010–1021.
47 J. M. Shen, W. J. Tang, X. L. Zhang, T. Chen and H. X. Zhang, *Carbohydr. Polym*, 2012, **88**, 239–249.

48 S. S. Dhaneshwar, M. Kandpal, N. Gairola and S. S. Kadam, *Indian J. Pharm. Sci.*, 2006, **68**(6), 705.
49 G. Kumar, R. K. Kotnala, J. Shah, V. Kumar, A. Kumar, P. Dhimana and M. Singhd, *Phys. Chem. Chem. Phys.*, 2017, **19**, 16669–16680.
50 G. K. Williamson and W. H. Hall, *Acta Metall.*, 1953, **1**, 22.
51 K. V. Chandekar and K. M. Kant, *J. Mol. Struct.*, 2018, **1154**, 418–427.
52 R. Khenata, A. Bouhemadou, M. Sahnoun, A. H. Reshak, H. Baltache and M. Rabah, *Comput. Mater. Sci.*, 2006, **38**, 29–38.
53 T. R. Bastami, M. H. Entezari, Q. H. Hu, S. B. Hartono and S. Z. Qiao, *Chem. Eng. J.*, 2012, **210**, 157–165.
54 K. Huseyin, B. Abdulhadi, T. Muhammet, S. K. Yuksel, S. Murat and A. Bekir, *J. Alloys Compd.*, 2009, **479**, 49–55.
55 M. Satalkar, S. N. Kane, A. Ghosh, N. Ghodke, G. Barrera, F. Celegato, M. Coisson, P. Tiberto and F. Vinai, *J. Alloys Compd.*, 2014, **615**, S313–S316.
56 Z. Karimi, Y. Mohammadifar, H. Shokrollahi, S. Khameneh Asl, G. Yousefi and L. Karimi, *J. Magn. Magn. Mater.*, 2014, **361**, 150–156.
57 G. Kumar, R. K. Kotnala, J. Shah, V. Kumar, A. Kumar, P. Dhimana and M. Singhd, *Phys. Chem. Chem. Phys.*, 2017, **19**, 16669–16680.
58 A. A. Zarandi, A. A. S. Alvani, R. Salimi, H. Sameie, S. Moosakhani, D. Poelman and F. Rosei, *J. Mater. Chem. C*, 2015, **3**, 3935.
59 E. K. Lim, E. Jang, B. Kim, J. Choi, K. Lee, J. Suck Suh, Y. M. Huh and S. Haam, *J. Mater. Chem.*, 2011, **21**, 12473.
60 K. Sooklal, B. S. Cullum, S. M. Angel and C. J. Murphy, *J. Phys. Chem.*, 1996, **100**, 4551.
61 W. G. Becker, *J. Phys. Chem.*, 1983, **87**, 4888.
62 K. V. Anand, R. Mohan, M. Karl Chinnu and R. Jayavel, *Proc. Indian Natl. Sci. Acad.*, 2013, **79**, 395–399.
63 X. Wen, P. Zhang, T. A. Smith, R. J. Anthony, U. R. Kortshagen, P. Yu, Yu Feng, S. Shrestha, G. Coniber and S. Huang, *Sci. Rep.*, 2015, **5**, 12469.
64 A. G. Kolhatkar, A. C. Jamison, D. Litvinov, R. C. Willson and T. R. Lee, *Int. J. Mol. Sci.*, 2013, **14**, 5977–6009.
65 P. Guardia, A. Labarta and J. Batlle, *J. Phys. Chem. C*, 2011, **115**, 390–396.
66 P. Seal, N. Paul, P. D. Babu and J. P. Borah, *Appl. Phys. A: Solids Surf.*, 2019, **125**, 290.
67 K. Lina and S. Oumarou, *Prog. Biomater.*, 2016, **5**, 147–160.
68 B. K. Mujasum, R. Emadh, Y. Yujie, A. S. Farooq, K. Mujeeb and I. Ahmeed, *AIP Adv.*, 2019, 55202.
69 H. B. Callen, S. E. Harisson and C. J. Kriessman, Cation distribution in ferro-spinels, *Theor. Phys. Rev.*, 1956, **103**, 851–856.
70 C. N. Chinnasamy, B. Jeyadevan, K. Shinoda, K. Tohji and D. J. Djayaprawira, *Appl. Phys. Lett.*, 2003, **83**, 2862.
71 Y. Eom, M. Abbas, H. Y. Noh and C. G. Kim, *RSC Adv.*, 2016, **6**, 15861–15867.
72 X. Fan, J. Guan, X. Cao, W. Wang and F. Mou, *Eur. J. Inorg. Chem.*, 2010, **40**, 419–426.
73 A. Muela, D. Muñoz, R. Martín-Rodríguez, I. Orue, E. Garaio, A. A. Díaz de Cerio, J. Alonso, J. A. García, M. Luisa and F. Gubieda, *J. Phys. Chem. C*, 2017, **120**, 24437–24448.
74 R. Hergt and S. Dutz, *J. Magn. Magn. Matter*, 2007, **311**, 187–192.
75 S. Bae, S. Won Lee, Y. Takemura, E. Yamashita, J. Kunisaki, S. Zurn and C. Sung Kim, *IEEE Trans. Magn.*, 2006, **42**, 10.
76 R. R. Wildeboer, P. Southern and Q. A. Pankhurst, *J. Phys. D: Appl. Phys.*, 2014, **47**, 495003.
77 D. K. Mondal, C. Borgohain, N. Paul and J. P. Borah, *Phys. B*, 2019, **567**, 122–128.
78 A. E. Deatsch and B. A. Evans, *J. Magn. Magn. Mater.*, 2014, **354**, 163–172.
79 A. Aharoni, *Introduction to the Theory of Ferromagnetism*, Clarendon Press, 2000.
80 K. Wu and J. P. Wang, *AIP Adv.*, 2017, **7**, 056327.
81 A. Weizenmann, M. Santos and W. Figueiredo, *Phys. Lett. A*, 2012, **376**, 1535–1539.
82 L. C. Branquinho, M. S. Carrião, A. S. Costa, N. Zufelato, M. H. Sousa, R. Miotto, R. Ivkov and A. F. Bakuzis, *Sci. Rep.*, 2013, **3**, 2887.
83 D. F. Coral, P. Mendoza Zélis, M. Marciello, M. P. Morales, A. Craievich, F. H. Sánchez and M. B. Fernández van Raap, *Langmuir*, 2016, **32**, 1201–1213.
84 R. D. Raland, D. Saikia, C. Borgohaina and J. P. Borah, *J. Phys. D: Appl. Phys.*, 2017, **50**, 325004.
85 L. Zeng, W. Ren, J. Zheng, P. Cui and A. Wu, *Phys. Chem. Chem. Phys.*, 2012, **14**, 2631–2636.
86 D. C. Chan, D. B. Kirpotin and P. A. Bunn Jr, *J. Magn. Magn. Mater.*, 1993, **122**, 374.
87 C. H. Li, P. Hodgins and G. P. Peterson, *J. Appl. Phys.*, 2011, **110**, 054303.
88 E. C. Abenojar, S. Wickramasinghi and J. Bas-Conception, *Prog. Nat. Sci.: Mater. Int.*, 2016, **26**, 440–448.